

Three-dimensional dynamic rupture simulation with a high-order discontinuous Galerkin method on unstructured tetrahedral meshes

Christian Pelties,¹ Josep de la Puente,² Jean-Paul Ampuero,³ Gilbert B. Brietzke,⁴ and Martin Käser⁵

Received 8 September 2011; revised 30 December 2011; accepted 6 January 2012; published 18 February 2012.

[1] Accurate and efficient numerical methods to simulate dynamic earthquake rupture and wave propagation in complex media and complex fault geometries are needed to address fundamental questions in earthquake dynamics, to integrate seismic and geodetic data into emerging approaches for dynamic source inversion, and to generate realistic physics-based earthquake scenarios for hazard assessment. Modeling of spontaneous earthquake rupture and seismic wave propagation by a high-order discontinuous Galerkin (DG) method combined with an arbitrarily high-order derivatives (ADER) time integration method was introduced in two dimensions by de la Puente et al. (2009). The ADER-DG method enables high accuracy in space and time and discretization by unstructured meshes. Here we extend this method to three-dimensional dynamic rupture problems. The high geometrical flexibility provided by the usage of tetrahedral elements and the lack of spurious mesh reflections in the ADER-DG method allows the refinement of the mesh close to the fault to model the rupture dynamics adequately while concentrating computational resources only where needed. Moreover, ADER-DG does not generate spurious high-frequency perturbations on the fault and hence does not require artificial Kelvin-Voigt damping. We verify our three-dimensional implementation by comparing results of the SCEC TPV3 test problem with two well-established numerical methods, finite differences, and spectral boundary integral. Furthermore, a convergence study is presented to demonstrate the systematic consistency of the method. To illustrate the capabilities of the high-order accurate ADER-DG scheme on unstructured meshes, we simulate an earthquake scenario, inspired by the 1992 Landers earthquake, that includes curved faults, fault branches, and surface topography.

Citation: Pelties, C., J. de la Puente, J.-P. Ampuero, G. B. Brietzke, and M. Käser (2012), Three-dimensional dynamic rupture simulation with a high-order discontinuous Galerkin method on unstructured tetrahedral meshes, *J. Geophys. Res.*, 117, B02309, doi:10.1029/2011JB008857.

1. Introduction

[2] Strong ground motion simulations of earthquakes require, in order to describe natural phenomena, the proper description and modeling of several features, e.g., seismic source representation, geometry of fault systems, material properties of the bedrock and sediment, topography. A highly

accurate solution of the resulting wavefield is also essential. The seismic source can be described through a prescribed evolution of slip along the fault or by prescribing physical criteria for earthquake rupture and letting the fault slip be a spontaneous consequence of the state of the fault. The two approaches are called kinematic and dynamic fault representation, respectively. The advantage of dynamic source modeling is that one can investigate how the fault interacts with the surrounding conditions such as confining stress, free surface, or transient wavefields. Furthermore, the influence on the rupture process of the fault geometry and potential heterogeneities are taken into account. As a drawback, dynamic rupture modeling is much more challenging computationally and suffers from large uncertainties on the underlying physics.

[3] Many numerical algorithms have been tested in the past to model dynamic earthquake rupture, such as finite differences (FD) [e.g., Andrews, 1973; Day, 1982; Madariaga et al., 1998; Andrews, 1999; Day et al., 2005; Dalguer and

¹Geophysics Section, Department of Earth and Environmental Sciences, Ludwig-Maximilians-University, Munich, Germany.

²Department of Computer Applications in Science and Engineering, Barcelona Supercomputing Center, Barcelona, Spain.

³Seismological Laboratory, California Institute of Technology, Pasadena, California, USA.

⁴Department of Physics of the Earth, German Research Centre for Geosciences, Potsdam, Germany.

⁵Geo Risks Research, Münchener Rückversicherungs-Gesellschaft, Munich, Germany.

Day, 2007; Moczo et al., 2007], boundary integral (BI) [e.g., Das, 1980; Andrews, 1985; Cochard and Madariaga, 1994; Geubelle and Rice, 1995; Lapusta et al., 2000; Tada and Madariaga, 2001], finite volume (FV) [e.g., Benjema et al., 2007, 2009], finite element (FE) [e.g., Oglesby et al., 1998, 2000; Aagaard et al., 2001; Galis et al., 2008], or spectral element (SE) [e.g., Ampuero, 2002; Vilotte et al., 2006; Kaneko et al., 2008; Galvez et al., 2011] methods. All these methods provide certain advantages, but have also disadvantages. For instance, FD schemes can be implemented efficiently to solve very large problems but have difficulties in modeling nonplanar faults and strong material contrasts, like in sedimentary basins with extremely low wave velocities, which require grid adaptivity. The BI method is one of the most accurate and computationally efficient methods but is impractical in heterogeneous media and non-linear materials. FV and FE methods can be implemented on unstructured meshes, which gives flexibility to describe realistic fault and crustal model geometries. However, they are usually formulated as low-order accurate operators that are very dispersive, which affects the small-scale resolution in the near-field and in turn the rupture front evolution. In contrast, SE methods are high-order accurate for seismic wave propagation, but are limited to hexahedral elements, which penalizes geometrical flexibility: it remains challenging to generate hexahedral meshes for complex three-dimensional branched fault systems with smooth element refinement or coarsening that adapts to material properties. Furthermore, all approaches suffer from spurious high-frequency oscillations, most notably in the slip rate time series. Several approaches have been proposed in order to reduce these oscillations, e.g., spatial low-pass filtering [Ampuero, 2002], absorption by a frequency-selective perfectly matched layer surrounding the fault [Festa and Vilotte, 2005, 2006], adding an ad hoc Kelvin-Voigt damping term to the solution [Day et al., 2005], or adaptive smoothing algorithms [Galis et al., 2010]. None of these solutions is completely satisfactory and high-frequency oscillations remain an unsolved nuisance in the numerical modeling of dynamic rupture.

[4] A new approach to overcome these issues was first presented by de la Puente et al. [2009]. They incorporated the earthquake source physics into a discontinuous Galerkin (DG) scheme linked to an arbitrary high-order derivatives (ADER) time integration [Titarev and Toro, 2002; Käser and Iske, 2005; Dumbser and Käser, 2006]. The DG method combines ideas from FE methods, where a polynomial basis approximates the physical variables of the elastic wave equations inside each element, and FV methods, introducing the desired concept of numerical fluxes. In addition to providing a high-order accurate approximation of the physical variables, the flux concept favors data locality: the temporal update of the solution inside one element depends only on its direct neighbors. Therefore, the method is well suited for massively parallel high-performance facilities. This formulation enables the use of fully unstructured meshes, i.e., triangles (2-D) or tetrahedrons (3-D), to better represent the geometrical constraints of a given geological setting and in particular the fault. The fault is honored by the mesh and can be sampled with small elements in order to capture small-scale rupture phenomena. Fast mesh coarsening

with increasing distance from the fault reduces the computational cost without introducing significant spurious grid reflections. Between any two elements the approximated variables of the elastic wave equation are discontinuous in a DG discretization. In our case, fluxes are defined by the exact solution of the elastic wave equations at a discontinuity (Godunov state) to exchange information between elements. Such kind of problem is known as the Riemann problem [Toro, 1999; LeVeque, 2002]. At a fault, de la Puente et al. [2009] showed how the exact solution of the Godunov state has to be modified to take the frictional boundary conditions into account. An important result of their study was that the ADER-DG solution is very smooth and free of spurious high-frequency oscillations. Therefore, it does not require artificial Kelvin-Voigt damping or filtering. The good numerical dispersion properties of the ADER-DG method [Dumbser et al., 2006; Käser et al., 2008; Hu et al., 1999; Sherwin, 2000], the possibility of using unstructured meshes [Pelties et al., 2010], and the natural representation of variables' discontinuities with Godunov fluxes [de la Puente et al., 2009] might be key features for accurate and efficient dynamic rupture simulations in very complex scenarios.

[5] The main goal of this paper is the extension of the ADER-DG rupture modeling scheme to three-dimensional problems on tetrahedral meshes. We present the Riemann problem for the three-dimensional case and show how its solution is used to compute high-order accurate numerical fluxes. We further use these fluxes together with a DG discretization of the elastodynamic system to build up a highly accurate fault modeling and wave propagation algorithm. The accuracy and convergence properties of the method are shown in convergence tests. Further verification is obtained by comparing the results of our novel 3-D DG dynamic rupture scheme with other well-established numerical solutions in a standard community test problem of fault rupture. Finally, a large earthquake simulation including complex fault systems, inspired from the 1992 Landers earthquake, shows the potential of the method in dealing with complicated geometrical constraints both in the rupture process and in the wave propagation itself.

2. Dynamics of Fault Rupture

[6] In the classical three-dimensional dynamic rupture models considered here a fault is represented by a 2-D plane of arbitrary shape (or a set of planes in a fault system with branches) across which fault coplanar displacements can be discontinuous. The kinematics of the sliding process are described by the spatiotemporal distribution of the slip vector $\Delta \mathbf{d} = \mathbf{d}^+ - \mathbf{d}^-$, or the slip rate vector $\Delta \mathbf{v} = \Delta \dot{\mathbf{d}}$, where \mathbf{d}^\pm are the displacements on each side of the fault, in the directions tangential to the fault plane (see Figure 1a). Earthquakes may involve small-scale fault opening, especially at shallow depth but, for simplicity, here we consider only examples in which both sides of the fault remain in contact. On any point of the fault surface, $\sigma_n > 0$ represents the compressive normal stress and $\boldsymbol{\tau}$ the shear traction vector resolved on the positive side of the fault. The dynamics of the sliding process are governed by friction relations between traction and slip [Andrews, 1976a, 1976b; Day

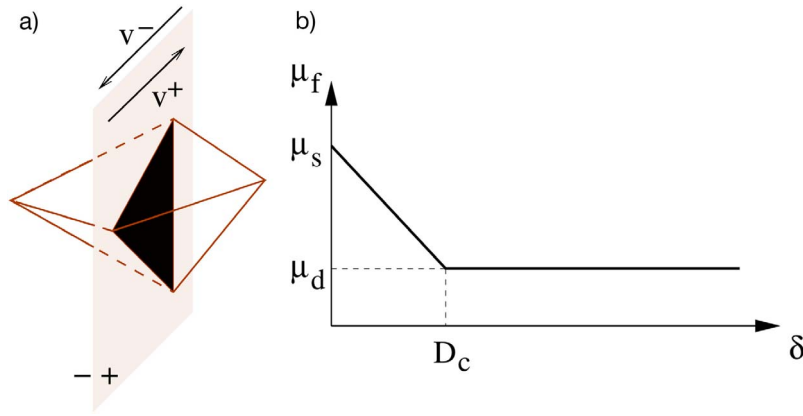


Figure 1. (a) A fault segment discretized as the contact surface of two tetrahedral elements. The different fault sides are indicated by plus and minus. (b) Plot of the friction coefficient μ_f versus the slip δ for the linear slip weakening friction law.

et al., 2005]. The shear traction is bounded by the fault strength, τ_s , which is proportional to the normal stress via the friction coefficient μ_f :

$$\tau_s = \mu_f \sigma_n. \quad (1)$$

Active slip requires the shear traction to reach and remain at the fault strength level, with a direction antiparallel to the slip rate. These conditions are encapsulated in the following equations for Coulomb friction:

$$\begin{aligned} |\tau| &\leq \tau_s, \\ (|\tau| - \tau_s)|\Delta \mathbf{v}| &= 0, \\ \Delta \mathbf{v}|\tau| + |\Delta \mathbf{v}|\tau &= 0. \end{aligned} \quad (2)$$

[7] The evolution of the friction coefficient with ongoing slip is described by the following linear slip weakening friction law:

$$\mu_f = \begin{cases} \mu_s - \frac{\mu_s - \mu_d}{D_c} \delta & \text{if } \delta < D_c, \\ \mu_d & \text{if } \delta \geq D_c, \end{cases} \quad (3)$$

where $\delta(t) = \int_0^t |\Delta \mathbf{v}| dt'$ is the slip path length. With increasing δ the friction coefficient μ_f drops linearly from the static value μ_s to the dynamic value μ_d over the critical slip distance D_c , as shown in Figure 1b. The linear slip weakening friction law is capable of modeling initial rupture, arrest of sliding and reactivation of slip. Since it is very simple and easy to implement, it is well suited to verifying numerical methods with dynamic rupture boundary condition. More advanced, realistic friction laws, incorporate rate-and-state effects [Dieterich, 1979; Ruina, 1983] and thermal phenomena such as flash heating and pore pressure evolution [Lachenbruch, 1980; Mase and Smith, 1985, 1987; Rice, 1999]. We do not expect any fundamental issue in the implementation of other friction laws in the ADER-DG method and leave that for future work.

3. Fault Dynamics Within the Discontinuous Galerkin Framework

[8] In contrast to other numerical dynamic rupture implementations, like the traction-at-split-node (TSN) approach [Andrews, 1973, 1999; Day, 1982], *de la Puente et al.* [2009]

followed a new idea employing the concept of fluxes. A detailed description of the adopted DG scheme is given by *Dumbser and Käser* [2006]. The mathematical and technical analysis of dynamic rupture boundary conditions in a high-order DG formulation was presented by *de la Puente et al.* [2009] in two dimensions. Therefore, in this section we explain only the basic ideas and show the extension to three-dimensional spontaneous rupture problems.

3.1. Discretization of the Linear Elastic Wave Equation

[9] The three-dimensional elastodynamic equations for an isotropic medium are written in velocity-stress form as the linear hyperbolic system

$$\begin{aligned} \frac{\partial}{\partial t} \sigma_{xx} - (\lambda + 2\mu) \frac{\partial}{\partial x} u - \lambda \frac{\partial}{\partial y} v - \lambda \frac{\partial}{\partial z} w &= 0, \\ \frac{\partial}{\partial t} \sigma_{yy} - \lambda \frac{\partial}{\partial x} u - (\lambda + 2\mu) \frac{\partial}{\partial y} v - \lambda \frac{\partial}{\partial z} w &= 0, \\ \frac{\partial}{\partial t} \sigma_{zz} - \lambda \frac{\partial}{\partial x} u - \lambda \frac{\partial}{\partial y} v - (\lambda + 2\mu) \frac{\partial}{\partial z} w &= 0, \\ \frac{\partial}{\partial t} \sigma_{xy} - \mu \left(\frac{\partial}{\partial x} v + \frac{\partial}{\partial y} u \right) &= 0, \\ \frac{\partial}{\partial t} \sigma_{yz} - \mu \left(\frac{\partial}{\partial z} v + \frac{\partial}{\partial y} w \right) &= 0, \\ \frac{\partial}{\partial t} \sigma_{xz} - \mu \left(\frac{\partial}{\partial z} u + \frac{\partial}{\partial x} w \right) &= 0, \\ \rho \frac{\partial}{\partial t} u - \frac{\partial}{\partial x} \sigma_{xx} - \frac{\partial}{\partial y} \sigma_{xy} - \frac{\partial}{\partial z} \sigma_{xz} &= 0, \\ \rho \frac{\partial}{\partial t} v - \frac{\partial}{\partial x} \sigma_{xy} - \frac{\partial}{\partial y} \sigma_{yy} - \frac{\partial}{\partial z} \sigma_{yz} &= 0, \\ \rho \frac{\partial}{\partial t} w - \frac{\partial}{\partial x} \sigma_{xz} - \frac{\partial}{\partial y} \sigma_{yz} - \frac{\partial}{\partial z} \sigma_{zz} &= 0, \end{aligned} \quad (4)$$

where λ is the first Lamé constant, μ is the shear modulus, ρ is the density, σ_{ij} are the components of the stress tensor and u , v and w are the components of the particle velocity in the x , y , and z directions, respectively. Grouping stresses and velocities into a vector $\mathbf{Q} = (\sigma_{xx}, \sigma_{yy}, \sigma_{zz}, \sigma_{xy}, \sigma_{yz}, \sigma_{xz}, u, v, w)^T$, we write the system of equations (4) in a more compact form:

$$\frac{\partial \mathbf{Q}_p}{\partial t} + A_{pq} \frac{\partial \mathbf{Q}_q}{\partial x} + B_{pq} \frac{\partial \mathbf{Q}_q}{\partial y} + C_{pq} \frac{\partial \mathbf{Q}_q}{\partial z} = 0, \quad (5)$$

where the space-dependent Jacobian matrices A , B and C include the material properties. Classical tensor notation and Einstein's summation convention are assumed.

[10] The computational domain Ω is divided into conforming tetrahedral elements $T^{(m)}$ identified by an index m . The physical variables \mathbf{Q} are approximated within each tetrahedral element $T^{(m)}$ by high-order polynomials

$$\mathcal{Q}_p^m(\boldsymbol{\xi}, t) = \hat{\mathcal{Q}}_{pl}^m(t) \Phi_l(\boldsymbol{\xi}), \quad (6)$$

where Φ_l are orthogonal basis functions and $\boldsymbol{\xi} = (\xi, \eta, \zeta)$ are the local coordinates in a canonical reference element T_E , where all the computations are done. Note, that we are using a modal basis formulation. The physical variables are expressed by a linear combination of these basis functions with time-dependent coefficients $\hat{\mathcal{Q}}_{pl}^m(t)$. The index p is associated with the unknowns in the vector \mathbf{Q} . The index l indicates the l th basis function and ranges from 0 to $L - 1$, where $L = (N + 1)(N + 2)(N + 3)/6$ is the number of required basis functions for a polynomial degree N . The numerical approximation order is $\mathcal{O} = N + 1$.

[11] The elastic wave equation is solved in the weak form. We multiply equation (5) by a test function Φ_k and integrate over an element $T^{(m)}$ and over a time increment of size Δt :

$$\begin{aligned} & \int_t^{t+\Delta t} \int_{T^{(m)}} \Phi_k \frac{\partial \mathcal{Q}_p}{\partial t} dV dt \\ & + \int_t^{t+\Delta t} \int_{T^{(m)}} \Phi_k \left(A_{pq} \frac{\partial \mathcal{Q}_q}{\partial x} + B_{pq} \frac{\partial \mathcal{Q}_q}{\partial y} + C_{pq} \frac{\partial \mathcal{Q}_q}{\partial z} \right) dV dt = 0. \end{aligned} \quad (7)$$

Integration by parts of equation (7) yields

$$\begin{aligned} & \int_t^{t+\Delta t} \int_{T^{(m)}} \Phi_k \frac{\partial \mathcal{Q}_p}{\partial t} dV dt + \sum_{j=1}^4 \mathcal{F}_{pk}^j \\ & - \int_t^{t+\Delta t} \int_{T^{(m)}} \left(\frac{\partial \Phi_k}{\partial x} A_{pq} + \frac{\partial \Phi_k}{\partial y} B_{pq} + \frac{\partial \Phi_k}{\partial z} C_{pq} \right) \mathcal{Q}_q dV dt = 0. \end{aligned} \quad (8)$$

Equation (8) provides the values of \mathcal{Q}_p at time $t + \Delta t$, following the procedures explained by Käser and Dumbser [2006] and Dumbser and Käser [2006]. They fully elaborated the integration of the first and third terms in equation (8). A thorough analysis of the used high-order accurate ADER time integration is given by Dumbser et al. [2006]. The second term is the sum of numerical fluxes \mathcal{F}_{pk}^j across the four faces of a tetrahedral element $j = 1, 2, 3, 4$, accounting for the discontinuity of \mathbf{Q} . This term achieves the exchange of information between elements. The incorporation of dynamic rupture boundary conditions is based on a modification of these fluxes. Thus, we will have a closer look at them in section 3.2.

3.2. Flux Computation

[12] For simplicity, we consider a single tetrahedral face with its normal aligned with the x axis. The flux term in (8) can then be written as

$$\mathcal{F}_{pk} = A_{pr} \int_t^{t+\Delta t} \int_S \Phi_k \tilde{\mathcal{Q}}_r dS dt, \quad (9)$$

where $\tilde{\mathbf{Q}}$ stands for a suitable approximation of the unknowns on the fault and the integral covers the face S and a time interval of size Δt . In order to solve the integrals numerically, we evaluate \mathbf{Q} at a set of space-time Gaussian integration points on the tetrahedral face at space locations $\boldsymbol{\xi}_i = (\xi_i, \eta_i, \zeta_i)$, with $i = 1, \dots, (N + 2)^2$, and along the time axis at time levels $\tau_l \in [t, t + \Delta t]$, with $l = 1, \dots, N + 1$. We define $\mathcal{Q}_{il} = \mathbf{Q}(\boldsymbol{\xi}_i, \tau_l)$ and $\mathcal{Q}_{p,il} = \mathcal{Q}_p(\boldsymbol{\xi}_i, \tau_l)$. We solve the flux locally at each space-time integration point while ensuring causality by updating the time levels in a sequential way. At special boundaries, such as the free surface or faults, the values of $\tilde{\mathbf{Q}}$ in (9) might be imposed in order to satisfy the physical boundary conditions. In the particular case of dynamic faults, we impose values derived from the Coulomb friction model (2).

[13] At a given time $\tau \in [t, t + \Delta t]$, a suitable temporal expansion of the variables is obtained via a Taylor expansion of order $\mathcal{O} = N + 1$ with respect to time t :

$$\mathcal{Q}_p(\boldsymbol{\xi}, \tau) \approx \sum_{k=0}^N \frac{(\tau - t)^k}{k!} \frac{\partial^k \mathcal{Q}_p(\boldsymbol{\xi}, t)}{\partial t^k}. \quad (10)$$

The high-order time derivatives in (10) are substituted by spatial derivatives using the expression (5) in an iterative way

$$\frac{\partial^k \mathcal{Q}_p(\boldsymbol{\xi}, t)}{\partial t^k} = (-1)^k \left(A_{pq} \frac{\partial}{\partial x} + B_{pq} \frac{\partial}{\partial y} + C_{pq} \frac{\partial}{\partial z} \right)^k \mathcal{Q}_q(\boldsymbol{\xi}, t). \quad (11)$$

This yields

$$\mathcal{Q}_p(\boldsymbol{\xi}, \tau) \approx \sum_{k=0}^N \frac{(\tau - t)^k}{k!} (-1)^k \left(A_{pq} \frac{\partial}{\partial x} + B_{pq} \frac{\partial}{\partial y} + C_{pq} \frac{\partial}{\partial z} \right)^k \mathcal{Q}_q(\boldsymbol{\xi}, t). \quad (12)$$

The expansion (12) provides a high-order prediction of the evolution of the degrees of freedom. We compute it at each time substep τ_l separately for the states $\mathbf{Q}^+(\boldsymbol{\xi}, t)$ and $\mathbf{Q}^-(\boldsymbol{\xi}, t)$ of the two elements on the positive and the negative side of the face across which the flux is evaluated (see Figure 1a). This yields predicted states \mathcal{Q}_{il}^+ and \mathcal{Q}_{il}^- .

[14] As mentioned above, between any two elements the variables of the elastic wave equations are in general discontinuous. A partial differential equation problem with discontinuous initial conditions is called a Riemann problem. The solution of the Riemann problem at an element interface is the Godunov state and can be written in terms of explicit values as [Toro, 1999; LeVeque, 2002; de la Puente et al., 2009]

$$\begin{aligned} 2\sigma_{xx,il}^G &= \left(\sigma_{xx,il}^+ + \sigma_{xx,il}^- \right) + \rho c_p (u_{il}^- - u_{il}^+), \\ 2\sigma_{xy,il}^G &= \left(\sigma_{xy,il}^+ + \sigma_{xy,il}^- \right) + \frac{\mu}{c_s} (v_{il}^- - v_{il}^+), \\ 2\sigma_{xz,il}^G &= \left(\sigma_{xz,il}^+ + \sigma_{xz,il}^- \right) + \frac{\mu}{c_s} (w_{il}^- - w_{il}^+), \\ 2u_{il}^G &= (u_{il}^+ + u_{il}^-) + \frac{1}{\rho c_p} (\sigma_{xx,il}^- - \sigma_{xx,il}^+), \\ 2v_{il}^G &= (v_{il}^+ + v_{il}^-) + \frac{c_s}{\mu} (\sigma_{xy,il}^- - \sigma_{xy,il}^+), \\ 2w_{il}^G &= (w_{il}^+ + w_{il}^-) + \frac{c_s}{\mu} (\sigma_{xz,il}^- - \sigma_{xz,il}^+). \end{aligned} \quad (13)$$

The stresses σ_{yy} , σ_{zz} , σ_{yz} are associated to the so-called zero wave speeds and do not contribute to the Godunov state. Equations (13) are readily evaluated based on the predicted states \mathbf{Q}_{il}^+ and \mathbf{Q}_{il}^- .

[15] When the fault is locked, the Godunov state is used in place of $\tilde{\mathbf{Q}}$ in the flux (9). When active slip is expected, we have to impose the shear stresses $\sigma_{xy,il}$ and $\sigma_{xz,il}$ on the fault according to the Coulomb friction model (2) to obtain new traction values $\tilde{\sigma}_{xy,il}$ and $\tilde{\sigma}_{xz,il}$, which might be different from $\sigma_{xy,il}^G$ and $\sigma_{xz,il}^G$. Note that fault-normal and fault-parallel components are uncoupled in equations (13). Because we ignore the possibility of fault opening, the Godunov state values are assigned to the fault-normal component of stress and velocity, $\tilde{\sigma}_{xx,il} = \sigma_{xx,il}^G$ and $\tilde{u}_{il} = u_{il}^G$. We can now evaluate the fault strength defined in equation (1):

$$\tau_s = \mu_{f,il} (\sigma_{xx,il}^G + \sigma_{xx,i}^0), \quad (14)$$

where the superscript zero denotes the initial stress values. The value of the friction coefficient is taken from the previous iteration and is updated later if active slip is detected.

[16] To solve for the friction conditions, we seek an independent relation between the fault-parallel variables of $\tilde{\mathbf{Q}}$ derived from the structure of the fluxes. Substituting $\sigma_{xy,il}^G$ and $\sigma_{xz,il}^G$ in equations (13) with their imposed values $\tilde{\sigma}_{xy,il}$ and $\tilde{\sigma}_{xz,il}$, then multiplying the second and third equations by c_s/μ and subtracting or adding the fifth and sixth equations, respectively, leads to

$$\begin{aligned} \tilde{v}_{il}^+ &= v_{il}^+ + \frac{c_s}{\mu} (\tilde{\sigma}_{xy,il} - \sigma_{xy,il}^+) \quad \text{and} \quad \tilde{v}_{il}^- = v_{il}^- - \frac{c_s}{\mu} (\tilde{\sigma}_{xy,il} - \sigma_{xy,il}^-), \\ \tilde{w}_{il}^+ &= w_{il}^+ + \frac{c_s}{\mu} (\tilde{\sigma}_{xz,il} - \sigma_{xz,il}^+) \quad \text{and} \quad \tilde{w}_{il}^- = w_{il}^- - \frac{c_s}{\mu} (\tilde{\sigma}_{xz,il} - \sigma_{xz,il}^-). \end{aligned} \quad (15)$$

These expressions are crucial for the understanding of fault dynamics using fluxes, as they state that an imposed shear traction instantly and locally generates an imposed velocity parallel to the fault. By subtracting them, the two components of slip rate are obtained:

$$\begin{aligned} \Delta \tilde{v}_{il} &= \frac{2c_s}{\mu} (\tilde{\sigma}_{xy,il} - \sigma_{xy,il}^G), \\ \Delta \tilde{w}_{il} &= \frac{2c_s}{\mu} (\tilde{\sigma}_{xz,il} - \sigma_{xz,il}^G). \end{aligned} \quad (16)$$

These expressions capture explicitly the analytical form of the immediate slip velocity response to changes in fault tractions, also known as radiation damping [Cochard and Madariaga, 1994; Geubelle and Rice, 1995]. A consequence of the equations in (16) is that slip (nonzero $\Delta \tilde{v}_{il}$ or $\Delta \tilde{w}_{il}$) occurs only if $\tilde{\sigma}_{xy,il} \neq \sigma_{xy,il}^G$ or $\tilde{\sigma}_{xz,il} \neq \sigma_{xz,il}^G$. The friction solver amounts to find the shear traction and slip rate (both vectors) that satisfy equations (2) and (16). The resulting algorithm is described next.

[17] We first test if the Godunov state satisfies the failure criterion

$$|\tau^G| \geq \tau_s, \quad (17)$$

where $|\tau^G| = \sqrt{(\sigma_{xy,il}^G + \sigma_{xy,i}^0)^2 + (\sigma_{xz,il}^G + \sigma_{xz,i}^0)^2}$. If this inequality is not satisfied, the fault is locked and the Godunov state values are assigned to all variables, $\tilde{\mathbf{Q}}_{il} = \mathbf{Q}_{il}^G$. Otherwise, active slip is declared and we compute $\tilde{\sigma}_{xy,il}$ and $\tilde{\sigma}_{xz,il}$ as

$$\begin{aligned} \tilde{\sigma}_{xy,il} &= \frac{\sigma_{xy,il}^G + \sigma_{xy,i}^0}{|\tau^G|} \tau_s, \\ \tilde{\sigma}_{xz,il} &= \frac{\sigma_{xz,il}^G + \sigma_{xz,i}^0}{|\tau^G|} \tau_s. \end{aligned} \quad (18)$$

[18] Next, the slip path length δ_{il} is obtained by integrating (16). Therefore, we apply the linear slip weakening friction law (3) to update the friction coefficient for the next iteration as

$$\mu_{f,il+1} = \max \left\{ \mu_d, \mu_s - \frac{\mu_s - \mu_d}{D_c} \delta_{il} \right\}. \quad (19)$$

Using the shear stresses $\tilde{\sigma}_{xy,il}$ and $\tilde{\sigma}_{xz,il}$ and the velocities from (15) all values of $\tilde{\mathbf{Q}}$ at the interface are known and the flux (9) can be computed with the discrete expression

$$\mathcal{F}_{pk} = A_{pr} \sum_{i=1}^{(N+2)^2} \sum_{l=1}^{N+1} \omega_i^S \omega_l^T \Phi_k(\xi_i) \tilde{\mathbf{Q}}_{r,il}, \quad (20)$$

where ω_i^S and ω_l^T are the weights of the spatial and temporal Gaussian integration, respectively.

4. Verification

[19] For geophysically relevant dynamic rupture problems no analytical solution exists that could be used as a reference for code verification. Therefore, the Southern California Earthquake Center (SCEC) created the Dynamic Earthquake Rupture Code Verification Exercise, in which different codes and methodologies are compared on a suite of benchmark problems of increasing complexity [Harris et al., 2009]. Here, we verify our method with the Test Problem Version 3 (TPV3). Additionally, in section 4.2 the convergence of the ADER-DG method is discussed.

4.1. Code Verification on the SCEC TPV3

[20] The TPV3 problem involves rupture on a 30 km long by 15 km deep vertical strike-slip fault embedded in a homogeneous elastic full space. The fault is governed by linear slip weakening friction and bounded by unbreakable barriers. The initial fault stresses are homogeneous except on a nucleation zone of higher initial shear stress (Figure 2). The friction parameters and background stresses can be found in Table 1. The medium has density $\rho = 2670 \text{ kg/m}^3$, P wave velocity $c_p = 6000 \text{ m/s}$ and S wave velocity $c_s = 3464 \text{ m/s}$. We use a conservatively large computational domain, a cube of edge length 72 km, to avoid spurious reflections from nonperfectly absorbing boundaries.

[21] We compare our $\mathcal{O}4$ ADER-DG solution with the results of the spectral boundary integral equation (SBIE)

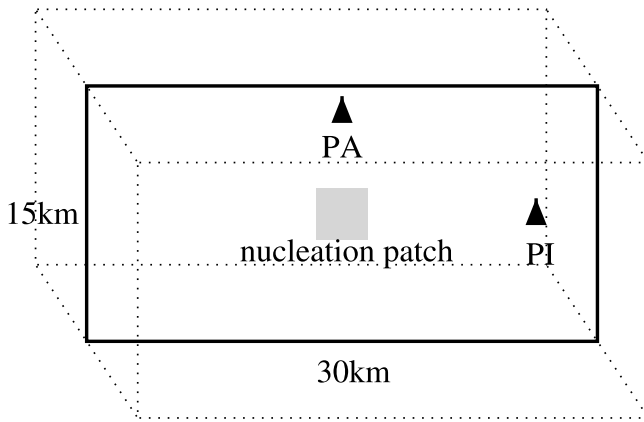


Figure 2. Sketch of the SCEC test case with the nucleation zone (shaded gray). The fault is surrounded by a box with an edge length of 72 km. The black triangles indicate the in-plane receiver (PI) and the antiplane receiver (PA).

method of *Geubelle and Rice* [1995] and of a second-order staggered grid finite difference method with traction at split nodes [Day *et al.*, 2005]. In particular, we considered two codes that have been verified during the SCEC exercises, the SBIE implementation of E. M. Dunham (MDSBI, Multi-dimensional spectral boundary integral, version 3.9.10, 2008, available at <http://pangea.stanford.edu/edunham/codes/codes.html>) and the finite difference code DFM (Dynamic Fault Model) of Day *et al.* [2005]. Both codes were run with a 50 m grid spacing. DFM incorporates artificial Kelvin-Voigt viscosity [Day and Ely, 2002].

[22] We discretize the model by an unstructured mesh of tetrahedra. The edge length on the fault plane is $h = 200$ m on average. We allow the size of the tetrahedral elements in the bulk to increase gradually to 3000 m edge length, to reduce the computational effort. No artificial reflections possibly caused by the mesh coarsening are observed. To facilitate a fair comparison between the methods, we define an equivalent mesh spacing $\Delta x = h(N + 1)$, which accounts for the subcell resolution of our high-order DG scheme. Although Δx is not consensually accepted as an exact measure of the spatial resolution, it is often used for comparing different discretization techniques. The relatively large element size of our ADER-DG simulation, $h = 200$ m, corresponds to an equivalent mesh spacing of $\Delta x = 50$ m, the same as in the DFM and MDSBI computations considered here.

[23] Figures 3a, 3b, 3c, and 3d show, for all three schemes, the time series of the shear stress and slip rate at the two fault locations indicated as PI and PA in Figure 2, which probe the in-plane and antiplane rupture fronts, respectively, at hypocentral distances of 7500 m and 6000 m, respectively. The ADER-DG solution (black) is in excellent agreement with the results produced by MDSBI (blue) and DFM (red). The signal amplitudes, the arrival time of the rupture front and stopping phases, and the subsequent stress relaxation are mutually consistent. A closer inspection of these results (Figures 3e and 3f) reveals that the rupture front arrives

slightly earlier in DFM than in the other two methods, whereas the rupture times of MDSBI and ADER-DG are more similar. These differences could be due to the Kelvin-Voigt damping in DFM or to different implementations of the nonsmooth initial stress conditions.

[24] Spurious high-frequency oscillations are visible in the slip rates produced by MDSBI and DFM, especially around the slip rate peak at the PA station. These are identified clearly in the spectra in Figures 3g and 3h: the MDSBI slip rates have a significant spectral peak around 25 Hz, and DFM has peaks between 10 and 40 Hz, especially at PA. Such spurious peaks are absent from the slip rate spectra of ADER-DG, which are smoother and follow the theoretically expected frequency decay [Ida, 1973]. Therefore, no artificial Kelvin-Voigt damping has to be applied in ADER-DG, which would further reduce the time step size and increase the computational cost. Our DG method is based on upwind numerical fluxes, which are intrinsically dissipative. In particular, in our high-order DG approach the amount of numerical dissipation increases very steeply as a function of frequency, beyond an effective high-frequency cutoff that depends on the element size [Hesthaven and Warburton, 2008, p. 90, Figure 4.1]. Hence, the very short wavelengths that are poorly resolved by the mesh elements are adaptively damped without perturbing the longer, physically meaningful wavelengths. The temporal discretization by the ADER scheme also introduces dissipation [Dumbser *et al.*, 2006] with a frequency cutoff that scales with the time step Δt . However, because Δt is global and controlled by the smallest or most deformed elements, the effect of this dissipation usually appears at much higher frequencies.

[25] The absence of spurious oscillations in ADER-DG enables the observation of interesting details of the solution. For instance, the ADER-DG solution reveals a slope discontinuity of the slip velocity shortly after the peak (at 3.15 s in Figure 3e and at 3.07 s in Figure 3f). This coincides with the time when the slip reaches D_c and is due to the slope discontinuity in the slip weakening friction law. In the other methods this feature is masked by the spurious oscillations.

4.2. Convergence Test

[26] In section 4.1 the good agreement between our ADER-DG method and other numerical methods has been shown. However, since there is no analytical solution available, one cannot determine which numerical method solves the proposed test better. A commonly used technique in computational science to verify the performance of a code is a convergence test. Thereby, we measure the error of the method by the root mean square (RMS) difference of rupture time, peak slip rate and final slip between the finest grid solution and the solutions for coarser grids. The particular

Table 1. Parameters Describing the Fault for the SCEC Test Case

Parameter	Nucleation Zone	Outside Nucleation Zone
Initial shear traction (MPa)	81.6	70.0
Initial normal stress (MPa)	120.0	120.0
Static friction coefficient	0.677	0.677
Dynamic friction coefficient	0.525	0.525
Critical slip distance (m)	0.4	0.4

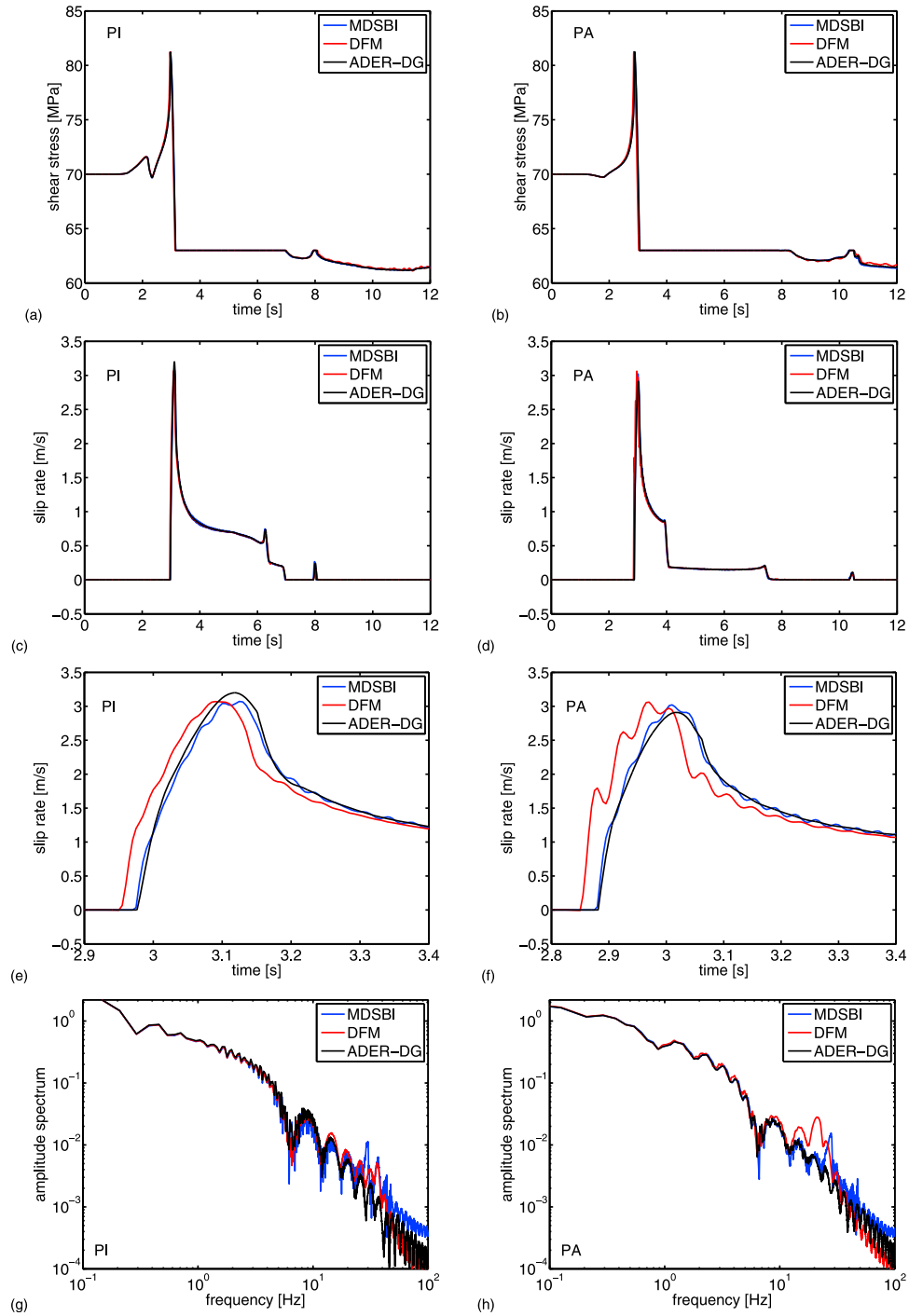


Figure 3. Comparison of solutions for the SCEC TPV3 problem obtained by different methods with comparable grid spacing: the boundary integral method (MDSBI, in blue) with a grid interval of $h = 50$ m, the FD staggered grid split node method (DFM, in red) with grid interval $h = 50$ m, and our ADER-DG scheme (in black) with an equivalent mesh spacing of $\Delta x = 50$ m at the fault. (a and b) The shear stresses and (c and d) the slip rates at two fault locations indicated as PI (Figures 3a, 3c, 3e, and 3g) and PA (Figures 3b, 3d, 3f, and 3h) in Figure 2. (e and f) A focused view of the slip rate peaks. (g and h) The spectra of the slip. All results are in good agreement. The ADER-DG solution does not produce spurious high-frequency oscillations.

Table 2. Convergence Results for the 3-D SCEC TPV3 Test Case

h (m)	\mathcal{O}	RMS Rupture Time (%)	RMS Final Slip (%)	RMS Peak Slip Rate (%)	CPU Time (s)
1061	4	2.79	2.88	14.52	2,288,640
	5	0.95	2.35	12.58	7,280,640
707	3	3.05	2.38	13.48	2,764,800
	4	0.74	1.85	11.39	8,386,560
	5	0.31	1.42	8.36	26,081,280
530	2	37.32	54.31	37.98	1,474,560
	3	1.44	1.61	10.84	4,945,920
	4	0.43	1.31	8.00	14,991,360
	5	0.19	1.22	6.87	49,827,840
424	2	15.34	39.62	25.84	2,580,480
	3	0.69	1.35	9.18	8,847,360
	4	0.20	1.20	6.76	29,675,520
	5	0.08	1.03	6.20	99,901,440
354	2	9.99	29.74	21.38	3,993,600
	3	0.44	1.20	7.65	14,499,840
	4	0.12	0.98	5.95	45,772,800
	5	0.04	1.03	5.84	163,553,280

RMS metrics we use in this chapter are taken from *Day et al.* [2005].

[27] We solved the SCEC TPV3 with five different mesh spacings, $h = 1061, 707, 530, 424$ and 354 m, defined as the longest triangular edge length on the fault plane, and four different orders of accuracy ranging from $\mathcal{O}2$ to $\mathcal{O}5$. The resolution of dynamic rupture problems can be quantified by N_c , the number of elements per median process zone length (here, 440 m [Day et al., 2005]). Our meshes correspond to $N_c = 0.41, 0.62, 0.83, 1.04$, and 1.24 , respectively. Some of the coarsest meshes at low orders lead to unphysical results and are ignored ($h = 707$ and 1061 m for $\mathcal{O}2$ and $h = 1061$ m for $\mathcal{O}3$). To facilitate comparisons between simulations of different resolution, we designed meshes that are uniform on the fault plane by first generating a regular surface mesh of quadrilateral elements of edge length $h/\sqrt{2}$, then dividing each quadrilateral into two triangles. In contrast, the tetrahedral mesh in the bulk is highly unstructured. We used mesh coarsening by increasing the element edge length by 10% per element with increasing distance from the fault, up to a maximum edge length of $10h$. The regular meshing of the fault plane does not affect the generality of our results: the accuracy of the simulation presented in section 4.1, executed on a fully unstructured mesh (irregular even on the fault plane), is consistent with the results presented hereafter. Our reference solution was obtained with $h = 354$ m and $\mathcal{O}6$. We sampled the solution with 400 randomly distributed receivers along the fault plane. The rupture time is defined as the first time sample at which the slip rate exceeds 1 mm/s. The 15 receivers located in the nucleation zone are excluded for the rupture time measurement since their rupture time is exactly the first time step.

[28] The results are summarized in Table 2 and visualized in Figure 4. The RMS difference in rupture time, final slip, and peak slip rate decrease with increasing mesh refinement and increasing order. This implies that a low-order approximation can achieve the accuracy of high-order approximations only when using a much smaller element size. Except for $\mathcal{O}2$, the RMS rupture time difference is low (Figure 4a),

and all chosen resolutions capture the rupture front evolution reasonably well with respect to the reference solution. The difference between the finest test solution and the reference solution is indeed very small, 0.04% (Table 2). The time step size Δt , shown by dashed lines in Figure 4a, is much smaller than the RMS rupture time differences; hence, temporal sampling does not bias our measurement of rupture times. The RMS difference of the final slip is also low, around 1% at best (Figure 4b). The RMS difference of peak slip rate is larger (Figure 4c), as usually found for this very sensitive error metrics based on extreme values of a spiky signal. Overall, the error levels are similar to those obtained by methods such as DFM [Day et al., 2005]. The ADER-DG solutions achieve numerical convergence with respect to the applied order and element size reduction.

[29] The convergence of the errors as a function of h is well described by power laws. The small scattering of the error data around their power law regressions (Figure 4) is expected when using structured mesh refinement strategies, like “red refinement” (split a triangle into four geometrically similar triangles), but is remarkable given our fully unstructured meshes. The smooth convergence to the reference solution confirms the robustness and reliability of the method. The exponent of the power laws, or convergence rate, is given in Table 3. The $\mathcal{O}2$ simulations achieve the highest convergence rates, but they also have the largest errors, as mentioned above. Between $\mathcal{O}3$ and $\mathcal{O}5$ the convergence rate saturates. This implies that spectral convergence is not achieved in this problem. In general, the convergence rate of a numerical solution improves when increasing the order of the method only if the exact solution is sufficiently smooth [Godunov, 1959; Krivodonova, 2007; Hesthaven and Warburton, 2008, p. 87]. Dynamic rupture problems contain nonsmooth features. Linear slip weakening friction guarantees continuity of slip velocity and shear stress, but slip acceleration remains singular at the leading and trailing edges of the process zone [Ida, 1973]. Moreover, the initial stress conditions and the stopping barriers are not smooth in the TPV3 problem. However, in smoother rupture problems involving rate-and-state friction and smooth initiation conditions, improvements of convergence rate with increasing order have not been observed [Rojas et al., 2009], only reduced rupture time errors below the time sampling precision [Kaneko et al., 2008]. In Table 3 the convergence rates of DFM and of a boundary integral method [from Day et al., 2005] are included for comparison. Whereas the convergence rates of the rupture time agree for the different methods, DFM and BI converge slightly faster than ADER-DG with $\mathcal{O} > 2$ for the other error metrics, final slip, and peak slip rate.

[30] Figure 4d shows the convergence of the rupture time misfit as a function of CPU time, the actual duration of the simulation multiplied by the number of processors involved. The number of processors ranges from 256 to 8192 since the problem size varies so much that the smallest simulation will not run efficiently on the maximum number of processors and the largest problem cannot be solved with fewer processors. Although the scalability of our DG code is in general good, it is still not perfect over this range of number of processors, which affects our measurements of CPU time. From Figure 4d higher-order methods are not more efficient

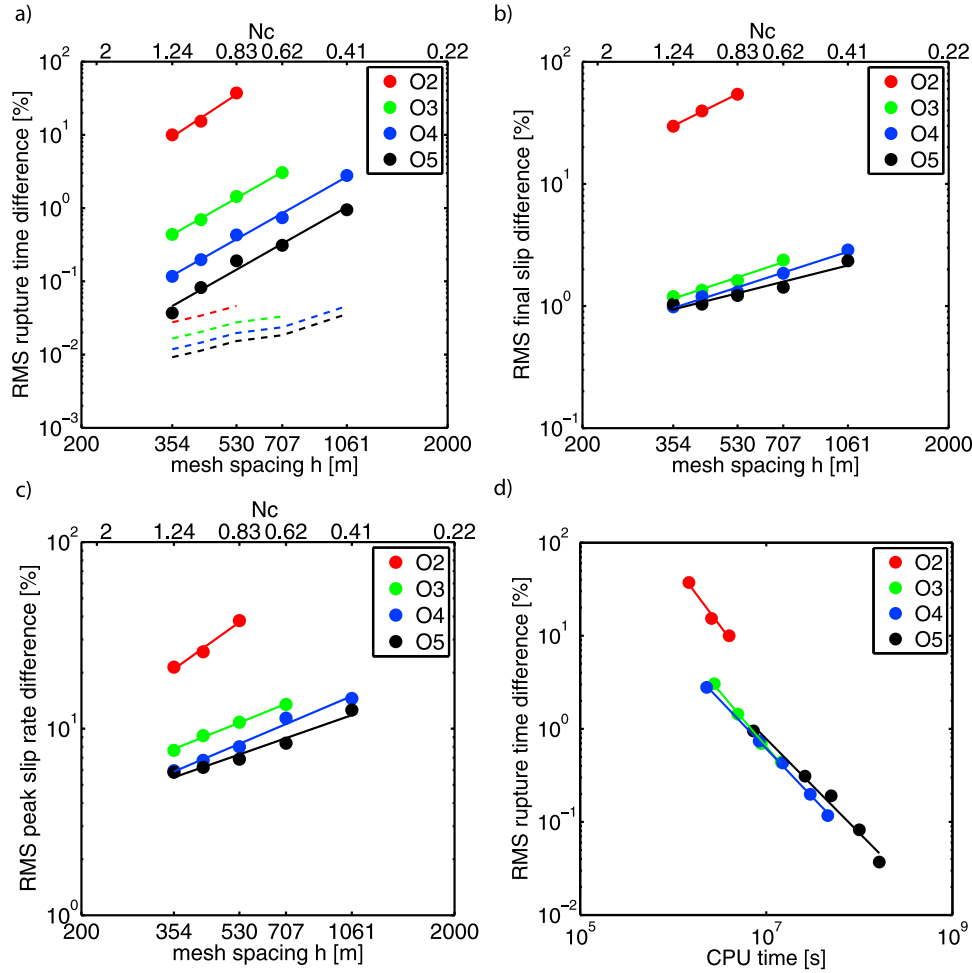


Figure 4. Convergence results for the 3-D SCEC TPV3 test case. N_c is the number of elements per median process zone length. Dots are the simulation results colored by their order of accuracy. The solid lines represent the regression, and the dashed lines denote the levels determined by the time step Δt . Misfits are shown for (a) the rupture time, (b) final slip, and (c) peak slip rate. (d) The convergence of the rupture time misfit as a function of its CPU time.

for solving the test problem at a given accuracy. For a given h , high-order methods are more computationally demanding as they store and update more unknowns per element, and this cost is not significantly offset by their improved accuracy. However, the smoothness of the slip rate time series (section 4.1) and the quality of the wave propagation away from the fault are not quantified by the error metrics considered here. Both aspects are an important part of the overall quality and accuracy of the solution. It has been demonstrated that a high-order approximation in a DG scheme is much more efficient for wave propagation problems than a low-order approximation; that is, it requires lower computational cost to achieve a given error level [Käser *et al.*, 2008]. The flexibility of the ADER-DG method allows the resolution to be optimized (h and p adaptivity) independently for the fault and for the surrounding media based on different criteria, the cohesive zone size and the maximum target frequency, respectively. A high-order approximation is advantageous in strong ground motion simulations based on dynamic rupture

scenarios because it provides an accurate wavefield at lower cost.

[31] For illustration purposes, we show time series of the shear stresses and slip rates used for the convergence test in Figure 5. The receiver has been picked randomly and is located at along-strike distance of 8525 m and downdip distance of 6893 m from the center of the nucleation zone. In

Table 3. Error Convergence Exponents for ADER-DG Schemes of Different Order

Method	Rupture Time	Final Slip	Peak Slip Rate
ADER-DG O2	3.28	1.48	1.43
ADER-DG O3	2.84	0.99	0.80
ADER-DG O4	2.83	0.97	0.85
ADER-DG O5	2.83	0.75	0.70
DFM ^a	2.96	1.58	1.18
BI ^a	2.74	1.53	1.19

^aThe convergence rates of DFM and BI are from Day *et al.* [2005].

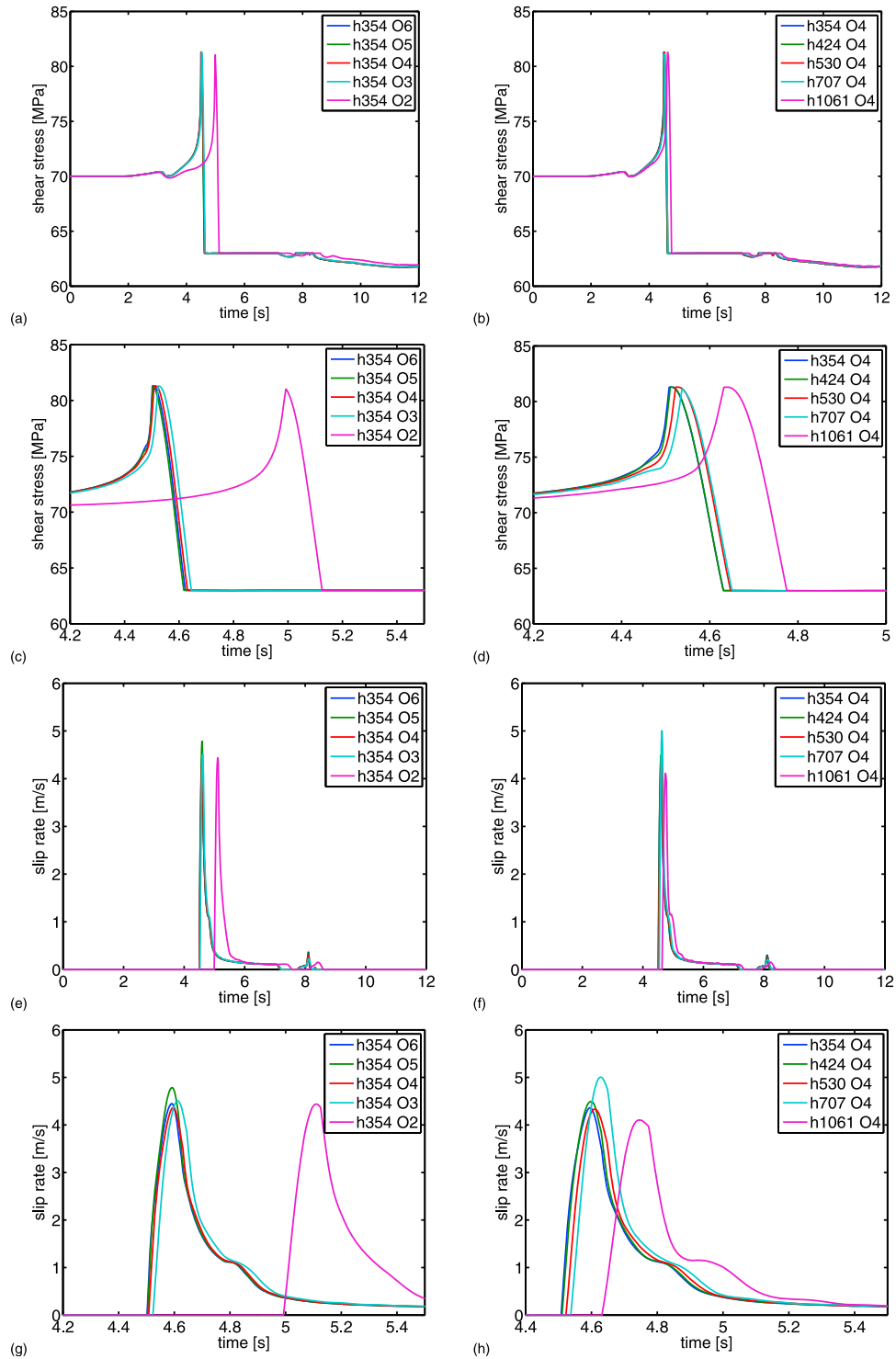


Figure 5. Representative solutions of the SCEC TPV3 problem with ADER-DG of varying grid spacing and order. (a and b) Shear stress and (e and f) slip rate at fault location at a distance of 8525 m along strike and 6893 m downdip from the center of the nucleation zone. (c, d, g, and h) Details near the rupture front. Figures 5a, 5c, 5e, and 5g show the results of all used orders of accuracy \mathcal{O} for a fixed mesh spacing $h = 354$ m, including the reference solution $\mathcal{O}6$. In Figures 5b, 5d, 5f, and 5h, the order is fixed to $\mathcal{O}4$ but the mesh spacing varies.

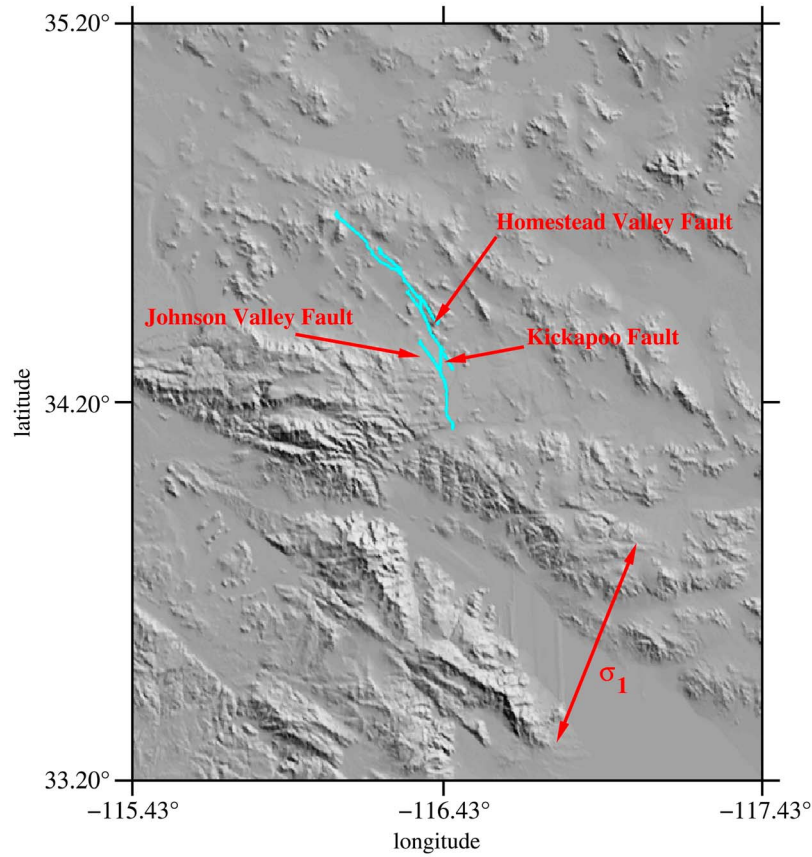


Figure 6. Map view of the 1992 Landers earthquake fault system with topography. The red double arrow indicates the assumed principal stress direction of N22°E. The lateral center of the model domain is the location of the epicenter at 34.20°N, 116.43°W.

Figures 5a, 5c, 5e, and 5g, results of all used orders of accuracy \mathcal{O} are given for a fixed mesh spacing $h = 354$ m. Note that \mathcal{O}_6 is our reference solution. In Figures 5b, 5d, 5f, and 5h, the order is fixed to \mathcal{O}_4 , but the mesh spacing varies. Obviously, the \mathcal{O}_2 simulation has the largest delay compared to the reference solution, explaining the large errors of the low-order runs. Also visible is a significant delay in the simulation with $h = 1061$ and \mathcal{O}_4 (Figures 5b, 5d, 5f, and 5h). The differences of all other simulations are only noticeable in the detail views of the rupture front (Figure 5c, 5d, 5g, and 5h). No spurious oscillations occur, independent of the mesh spacing and the order of accuracy. Furthermore, no artifacts of the high-order formulation (e.g., overshoots or undershoots) appear at the discontinuities.

5. The Landers 1992 Earthquake

[32] To demonstrate the potential of the introduced ADER-DG method on unstructured meshes for simulations of rupture dynamics in complex fault geometries, we consider the 28 June 1992 $M_w 7.3$ Landers, California, earthquake as an example. Our purpose here is not to reexamine the dynamics of this event in detail, as in many previous studies [e.g., Olsen *et al.*, 1997; Aochi and Fukuyama, 2002; Aochi *et al.*, 2003; Fliss *et al.*, 2005] but rather to

illustrate the potential of our method for future studies. We hence follow the simplified setup introduced by *de la Puente et al.* [2009] and extend it to three dimensions, including topography.

[33] The Landers earthquake occurred on a 60 km long complex fault system along the western edge of the Eastern California Shear Zone. Its surface rupture involved at least parts of four major right-lateral strike-slip fault segments, breaking successively from south to north the Johnson Valley, Homestead Valley, Emerson, and Camp Rock faults [Hauksson *et al.*, 1993]. These subparallel main segments are curved, overlapping, and connected by shorter faults (e.g., the Kickapoo, or Landers fault, connecting the Johnson Valley and Homestead Valley faults). A fault geometry comprising six nonplanar fault segments (Figure 6) was adopted from Aochi and Fukuyama [2002]. Studies based on guided waves [Li *et al.*, 1994] and analysis of the aftershock distribution [Hauksson *et al.*, 1993] show that the surface geometry continues to a depth of at least 10 km. Source inversion results indicate a vertical dip of the fault planes [Wald and Heaton, 1994; Cohee and Beroza, 1994; Cotton and Campillo, 1995]. We hence model the three-dimensional fault system geometry by extending the surface fault traces vertically into depth. The fault plane starts below the surface at sea level and extends to 15 km below

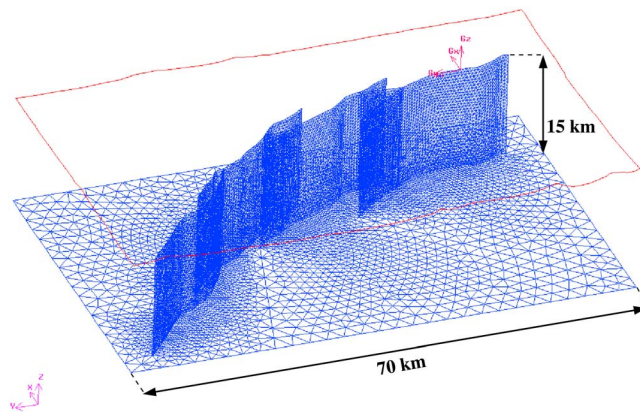


Figure 7. Discretization of the Landers fault system with triangles of 500 m edge length. In the area indicated by the red line the topography is described by a fine mesh of 500 m edge length. The box below is filled by 2500 m elements with only moderate mesh coarsening away from the fault.

sea level. Although we do not allow for surface rupture in this tentative test scenario, surface rupture was successfully verified with the current ADER-DG implementation with the SCEC TPV5. These data are freely available from the SCEC Web site (<http://scecddata.usc.edu/cvws/>).

[34] The model domain is a polygon of lateral extension of 180 km times 220 km and depth of 50 km. Figure 6 shows a map of the model area and its topography. The fault system is enclosed in the south by the San Bernardino mountains, with a maximum elevation of 3505 m and in the north by smaller dissected mountain ranges.

[35] Since our purpose is to focus on the rupture process on a geometrically complex fault system, we assume a homogeneous medium ($v_p = 6200$ m/s, $v_s = 3520$ m/s and $\rho = 2700$ kg/m³) and a homogeneous initial stress field with horizontal principal stresses $\sigma_1 = 300$ MPa and $\sigma_2 = 100$ MPa. The assumed direction of the largest principal stress, N22°E, is representative of the northern part of the rupture in the model of *Aochi and Fukuyama* [2002] and is indicated by a red double arrow in Figures 6 and 8a. Although the stress field is homogeneous, the varying fault strike generates a heterogeneous stress state along the fault. The nucleation is initiated by a lower principal stress value of $\sigma_2 = 70$ MPa in a square patch of edge length 3 km around the hypocenter, located on the southern portion of the Johnson Valley fault. Table 4 contains the frictional parameters of the fault. We compute the spontaneous rupture for a total duration of 10 s.

[36] Figure 7 shows the fault discretized by triangles of size $h = 500$ m (edge length). The horizontal plane below the fault shows the mesh coarsening up to $h = 2500$ m in the closer neighborhood of the fault. The surface mesh above the fault has $h = 500$ m to ensure an accurate representation of the topography. This high-resolution area is surrounded by a much coarser mesh consisting mainly of $h = 5$ km elements, but we allow for $h = 10$ km at the outer borders of the domain. The fast mesh coarsening does not affect the

rupture propagation, it only damps the high-frequency content of the wavefield in areas of larger mesh spacing [*de la Puente et al.*, 2009]. This allows concentration of the computational effort on the rupture area, where it is needed. The domain boundaries are located far enough away from the fault to avoid the effect of possible artificial reflections.

[37] The resulting mesh contains 587,585 elements. Using an $\mathcal{O}5$ approximation, this model size is relatively inexpensive and can be computed on a small-scale cluster of approximately 100 nodes, which can be currently found in many research institutions. We used the BlueGene/P machine Shaheen of the King Abdullah University of Science and Technology, Saudi Arabia. Our 10 s long simulation ran for 20 h on 512 processors. This relatively large number of processors was conditioned by the low frequency of the BlueGene/P CPUs (850 MHz), and for standard CPUs, it can be reduced by a factor of 4 to 6. The entire discretization process including topography and fault geometry definition, mesh generation, and boundary specifications took less than 2 days due to the flexibility and robustness of tetrahedral mesh generation. Hence, the manual effort and related cost in terms of expert working hours are kept at a minimum.

[38] Figure 8 shows the amplitude of the particle velocity generated by the earthquake at four different times on a horizontal cross section of the nucleation area at a depth of 5 km below sea level. Initially, the rupture propagates bilaterally on the Johnson Valley fault (Figure 8a). At time 1.5 s the northern rupture front approaches the first branching point (Figure 8b). It then continues into the Kickapoo fault, without breaking the northern portion of the Johnson Valley fault (Figure 8c). The rupture breaks the complete Kickapoo segment and continues on the Homestead Valley fault, where it stops approximately at time 6 s (Figure 8d). This rupture branching to the extensional side is consistent with the 2-D study of *de la Puente et al.* [2009] and with theoretical considerations [*Poliakov et al.*, 2002]. While some interesting features of the Landers earthquake rupture, like the backward branching to the southern segment of the Homestead Valley fault [*Poliakov et al.*, 2002; *Fliss et al.*, 2005], are not reproduced by our simulation, it achieves our main intention to conceptually illustrate the capabilities of the 3-D ADER-DG method.

[39] Figure 9 shows the surface wavefield developing with time from 2.5 s to 4.5 s. There is a clear directivity effect: most of the energy is traveling northward, like the rupture front. From visual inspection, the topography seems to increase the complexity of the wavefield. However, we expect stronger site effects when incorporating a more

Table 4. Frictional Parameters for the Test Case of the Landers Fault System

Parameter	Nucleation Zone	Outside Nucleation Zone
Principal stress σ_1 (MPa)	300.0	300.0
Principal stress σ_2 (MPa)	70.0	100.0
Static friction coefficient	0.6	0.6
Dynamic friction coefficient	0.4	0.4
Critical slip distance (m)	0.8	0.8

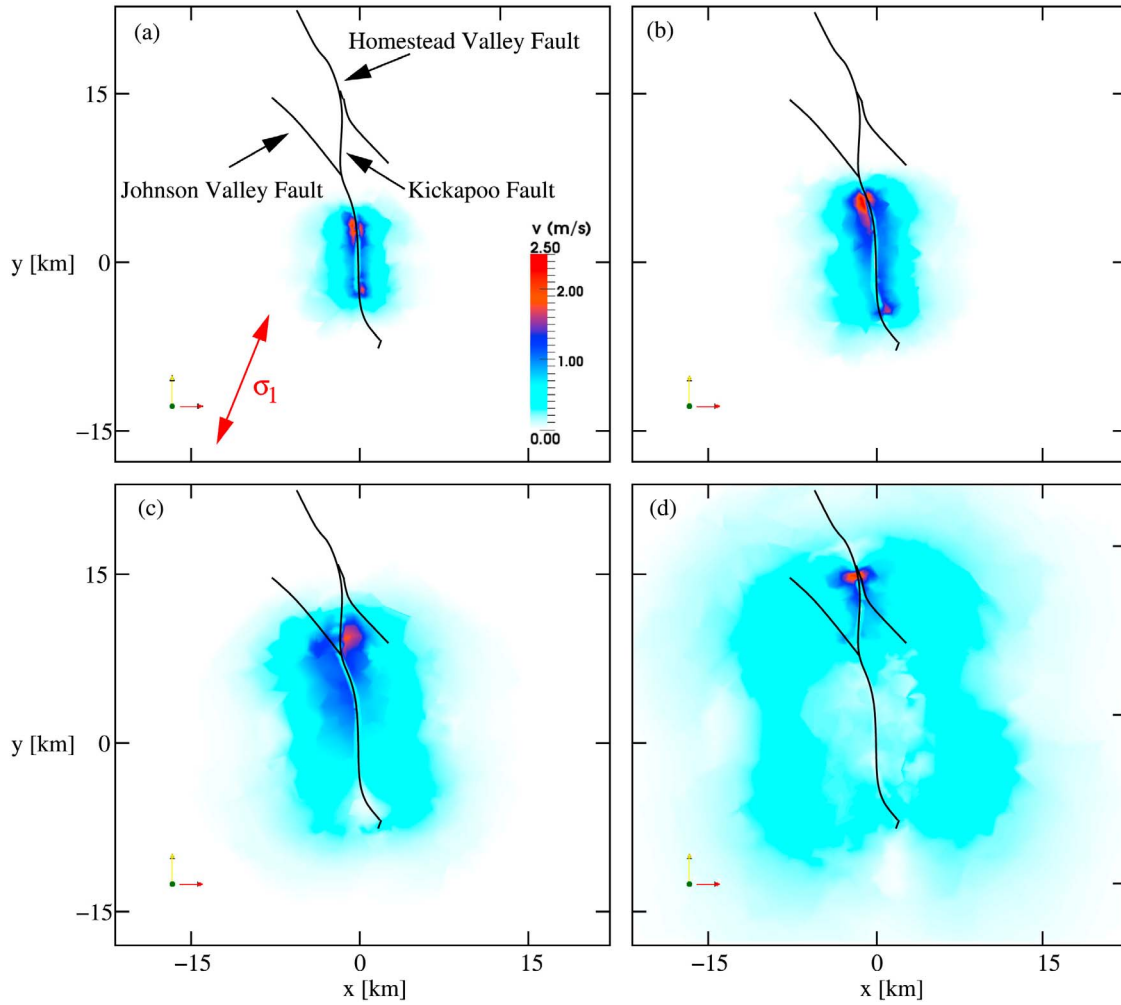


Figure 8. Snapshots of absolute particle velocity at (a) 1, (b) 1.5, (c) 2.5, and (d) 4.5 s after rupture initiation on a horizontal cut of the nucleation area at a depth of 5 km below sea level. The red double arrow in Figure 8a indicates the assumed principal stress direction.

realistic geological model with low-velocity layers in the valley and stiffer material in the mountains.

6. Conclusions

[40] We successfully incorporated 3-D earthquake rupture dynamics in the ADER-DG scheme by modifying the Riemann problem according to the Coulomb friction model. Although we considered here linear slip weakening friction, the method allows for the implementation of more advanced friction laws, e.g., rate-and-state friction. Accuracy was verified by comparing results of the SCEC TPV3 benchmark problem for spontaneous rupture to well-established methods. The ADER-DG solution is notably free of spurious high-frequency oscillations, most likely owing to the high-order frequency dependence of the intrinsic dissipation of the DG method. Hence, no further artificial viscous damping mechanism has to be applied which could potentially affect the rupture process. The robustness and systematic correctness of the ADER-DG method were proved by a

convergence test, which showed that mesh refinement or increasing the order leads to smaller errors.

[41] An example of dynamic rupture simulation on a complex fault system, inspired by the surface rupture geometry of the Landers earthquake, demonstrates the great benefits of the proposed method based on unstructured tetrahedral meshes that can be aligned into merging faults under shallow angles. Areas of interest, here the topography and the fault, can be modeled adequately by small elements, while mesh coarsening can be applied elsewhere to reduce the computational cost. This is of interest in particular for dynamic rupture studies which require a fine sampling of the fault in order to capture the cohesive zone for a correct simulation of the rupture process while adapting the resolution to the dispersion requirements of wave propagation at lower frequencies far from the fault. We do not observe any artificial reflection due to mesh coarsening in ADER-DG. In methods based on structured grids the mesh refinement is instead applied uniformly in the entire computational

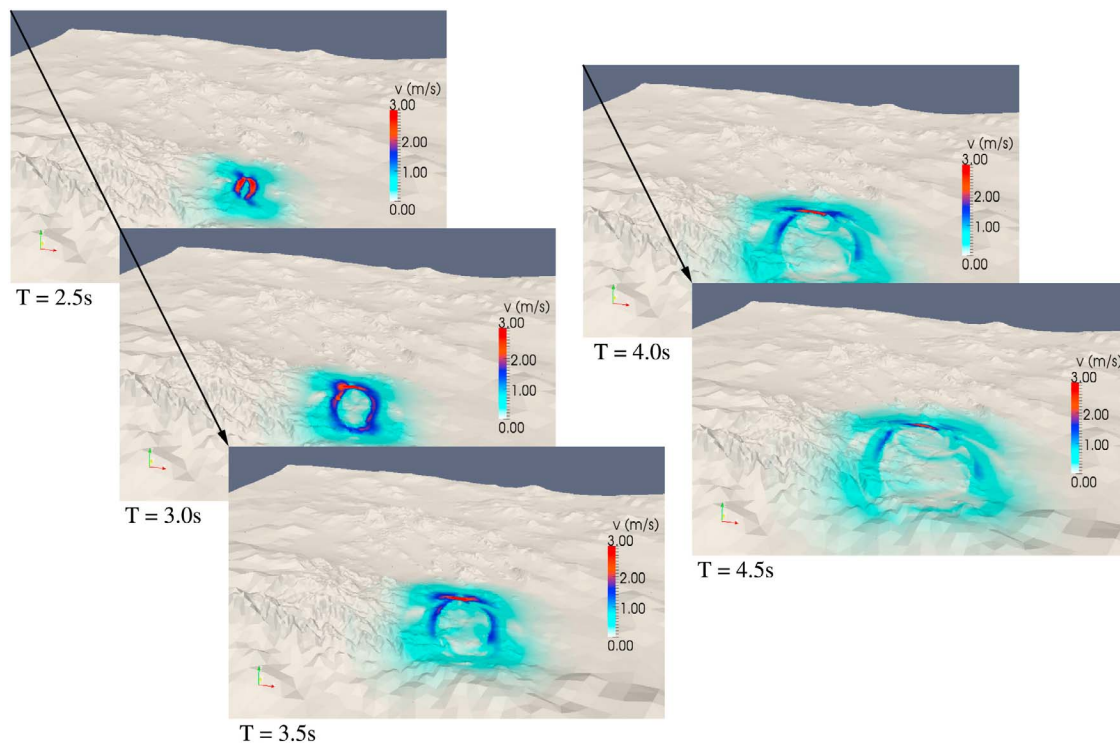


Figure 9. Development of the ground velocity field with time. The topography is scaled by a factor of 3; v represents the absolute particle velocity in m/s. The viewing direction is roughly from southeast to northwest. The directivity effect can be clearly observed.

domain, propagating frequencies much higher than required for strong ground motion investigations, or through grid-doubling techniques, which could generate artificial reflections.

[42] We conclude that the combination of meshing flexibility and high-order accuracy of the ADER-DG method will make it a very useful tool to study earthquake dynamics on complex fault systems. Future steps in the development include the incorporation of bimaterial fault interfaces, more realistic friction laws, and nonlinear bulk rheologies.

[43] **Acknowledgments.** The authors thank the DFG (Deutsche Forschungsgemeinschaft), as the work was supported through the Emmy Noether-Programm (KA 2281/2-1). J.-P. A. was partially funded by NSF (grant EAR-0944288) and by the Southern California Earthquake Center (funded by NSF Cooperative Agreement EAR-0106924 and USGS Cooperative Agreement 02HQAG0008). The DFM data used for comparison were provided by Luis A. Dalguer and the SBIEM solutions were produced with the code of Eric M. Dunham (MDSBI: Multidimensional spectral boundary integral, version 3.9.10, 2008, available at <http://pangea.stanford.edu/~edunham/codes/codes.html>). Furthermore, we thank Luis A. Dalguer and Alan Schiemenz for very helpful and fruitful discussions. Cristóbal E. Castro gave valuable comments and advice on the solution of the Riemann problem and the parallelization. We also thank M. Mai for providing computational resources as many parallel tests, the convergence test, and the SCEC benchmark have been computed on the BlueGene/P Shaheen of the King Abdullah University of Science and Technology, Saudi Arabia. This paper is SCEC contribution 1526 and Caltech Seismological Lab contribution 10067. The reviews and comments by J.-P. Vilotte, S. M. Day, and the Associate Editor are appreciated and helped us to improve the manuscript.

References

- Aagaard, B., T. Heaton, and J. Hall (2001), Dynamic earthquake rupture in the presence of lithostatic normal stresses: Implications for friction models and heat production, *Bull. Seismol. Soc. Am.*, **91**, 1765–1796.

- Ampuero, J.-P. (2002), Etude physique et numérique de la nucléation des séismes, Ph.D. thesis, Univ. Paris 7, Paris.
- Andrews, D. (1973), A numerical study of tectonic stress release by underground explosions, *Bull. Seismol. Soc. Am.*, **63**, 1375–1391.
- Andrews, D. (1976a), Rupture propagation with finite stress in antiplane strain, *J. Geophys. Res.*, **81**, 3575–3582.
- Andrews, D. (1976b), Rupture velocity of plane-strain shear cracks, *J. Geophys. Res.*, **81**, 5679–5687.
- Andrews, D. (1985), Dynamic plane-strain shear rupture with a slip-weakening friction law calculated by a boundary integral method, *Bull. Seismol. Soc. Am.*, **75**, 1–21.
- Andrews, D. (1999), Test of two methods for faulting in finite-difference calculations, *Bull. Seismol. Soc. Am.*, **89**, 931–937.
- Aochi, H., and E. Fukuyama (2002), Three-dimensional nonplanar simulation of the 1992 Landers earthquake, *J. Geophys. Res.*, **107**(B2), 2035, doi:10.1029/2000JB000061.
- Aochi, H., R. Madariaga, and E. Fukuyama (2003), Constraint of fault parameters inferred from nonplanar fault modeling, *Geochim. Geophys. Geosyst.*, **4**(2), 1020, doi:10.1029/2001GC000207.
- Benjemaa, M., N. Glinsky-Olivier, V. Cruz-Atienza, J. Virieux, and S. Piperno (2007), Dynamic non-planar crack rupture by a finite volume method, *Geophys. J. Int.*, **171**, 271–285.
- Benjemaa, M., N. Glinsky-Olivier, V. Cruz-Atienza, and J. Virieux (2009), 3-D dynamic rupture simulations by a finite volume method, *Geophys. J. Int.*, **178**, 541–560, doi:10.1111/j.1365-246X.2009.04088.x.
- Cochard, A., and R. Madariaga (1994), Dynamic faulting under rate-dependent friction, *Pure Appl. Geophys.*, **105**, 25,891–25,907.
- Cohee, B. P., and G. C. Beroza (1994), Slip distribution of the 1992 Landers earthquake and its implications for earthquake source mechanics, *Bull. Seismol. Soc. Am.*, **84**(3), 692–712.
- Cotton, F., and M. Campillo (1995), Frequency domain inversion of strong motions: Application to the 1992 Landers earthquake, *J. Geophys. Res.*, **100**, 3961–3975.
- Dalguer, L. A., and S. M. Day (2007), Staggered-grid split-node method for spontaneous rupture simulation, *J. Geophys. Res.*, **112**, B02302, doi:10.1029/2006JB004467.
- Das, S. (1980), A numerical method for determination of source time functions for general three-dimensional rupture propagation, *Geophys. J. R. Astron. Soc.*, **62**, 591–604.

- Day, S. (1982), Three-dimensional finite-difference simulation of fault dynamics: Rectangular faults with fixed rupture velocity, *Bull. Seismol. Soc. Am.*, **72**, 705–727.
- Day, S., and G. Ely (2002), Effect of a shallow weak zone on fault rupture: Numerical simulation of scale-model experiments, *Bull. Seismol. Soc. Am.*, **92**, 3022–3041.
- Day, S., L. Dalguer, N. Lapusta, and Y. Liu (2005), Comparison of finite difference and boundary integral solutions to three-dimensional spontaneous rupture, *J. Geophys. Res.*, **110**, B12307, doi:10.1029/2005JB003813.
- de la Puente, J., J.-P. Ampuero, and M. Käser (2009), Dynamic rupture modeling on unstructured meshes using a discontinuous Galerkin method, *J. Geophys. Res.*, **114**, B10302, doi:10.1029/2008JB006271.
- Dieterich, J. H. (1979), Modeling of rock friction 1. experimental results and constitutive equations, *J. Geophys. Res.*, **84**, 2161–2168, doi:10.1029/JB084iB05p02161.
- Dumbser, M., and M. Käser (2006), An arbitrary high order discontinuous Galerkin method for elastic waves on unstructured meshes II: The three-dimensional case, *Geophys. J. Int.*, **167**(1), 319–336.
- Dumbser, M., T. Schwartzkopff, and C.-D. Munz (2006), Arbitrary high order finite volume schemes for linear wave propagation, in *Computational Science and High Performance Computing II*, edited by E. Krause et al., pp. 129–144, Springer-Verlag, Berlin.
- Festa, G., and J.-P. Vilotte (2005), The Newmark scheme as velocity-stress time-staggering: an efficient PML implementation for spectral element simulations of elastodynamics, *Geophys. J. Int.*, **161**(3), 789–812, doi:10.1111/j.1365-246X.2005.02601.x.
- Festa, G., and J.-P. Vilotte (2006), Influence of the rupture initiation on the intersonic transition: Crack-like versus pulse-like modes, *Geophys. Res. Lett.*, **33**, L15320, doi:10.1029/2006GL026378.
- Fliss, S., H. S. Bhat, R. Dmowska, and J. R. Rice (2005), Fault branching and rupture directivity, *J. Geophys. Res.*, **110**, B06312, doi:10.1029/2004JB003368.
- Galis, M., P. Moczo, and J. Kristek (2008), A 3-D hybrid finite-difference-finite-element viscoelastic modelling of seismic wave motion, *Geophys. J. Int.*, **175**, 153–184.
- Galis, M., P. Moczo, J. Kristek, and M. Kristekova (2010), An adaptive smoothing algorithm in the TSN modeling of rupture propagation with the linear slip-weakening friction law, *Geophys. J. Int.*, **180**, 418–432.
- Galvez, P., J.-P. Ampuero, L. Dalguer, and T. Nissen-Meyer (2011), Dynamic rupture modelling of the 2011 M9 Tohoku earthquake with unstructured 3D spectral element method, Abstract U51B-0043 presented at 2011 Fall Meeting, AGU, San Francisco, Calif., 4–9 Dec., pp. Fall Meet. Suppl., Abstract S24.
- Geubelle, P., and J. Rice (1995), A spectral method for three-dimensional elastodynamic fracture problems, *J. Mech. Phys. Solids*, **43**, 1791–1824.
- Godunov, S. (1959), Finite difference method for numerical computation of discontinuous solutions of the equations of fluid dynamics, *Math. Sb.*, **47**, 271–306.
- Harris, R., et al. (2009), The SCEC/USGS Dynamic Earthquake Rupture Code verification exercise, *Seismol. Res. Lett.*, **80**(1), 119–126, doi:10.1785/gssrl.80.1.119.
- Hauksson, E., L. M. Jones, K. Hutton, and D. Eberhart-Phillips (1993), The 1992 Landers earthquake sequence: Seismological observations, *J. Geophys. Res.*, **98**, 19,835–19,858, doi:10.1029/93JB02384.
- Hesthaven, J., and T. Warburton (2008), *Nodal Discontinuous Galerkin Methods: Algorithms, Analysis, and Applications*, Springer, New York.
- Hu, F., M. Hussaini, and P. Rasetarinera (1999), An analysis of the discontinuous Galerkin method for wave propagation problems, *J. Comput. Phys.*, **151**, 921–946.
- Ida, Y. (1973), The maximum acceleration of seismic ground motion, *Bull. Seismol. Soc. Am.*, **63**, 959–968.
- Kaneko, Y., N. Lapusta, and J.-P. Ampuero (2008), Spectral element modeling of spontaneous earthquake rupture on rate and state faults: Effect of velocity-strengthening friction at shallow depths, *J. Geophys. Res.*, **113**, B09317, doi:10.1029/2007JB005553.
- Käser, M., and M. Dumbser (2006), An arbitrary high order discontinuous Galerkin method for elastic waves on unstructured meshes I: The two-dimensional isotropic case with external source terms, *Geophys. J. Int.*, **166**(2), 855–877.
- Käser, M., and A. Iske (2005), ADER schemes on adaptive triangular meshes for scalar conservation laws, *J. Comput. Phys.*, **205**, 486–508.
- Käser, M., V. Hermann, and J. de la Puente (2008), Quantitative accuracy analysis of the discontinuous Galerkin method for seismic wave propagation, *Geophys. J. Int.*, **173**(3), 990–999.
- Krivodonova, L. (2007), Limiters for high-order discontinuous Galerkin methods, *J. Comput. Phys.*, **226**, 879–896.
- Lachenbruch, A. H. (1980), Frictional heating, fluid pressure and the resistance to fault motion, *J. Geophys. Res.*, **85**, 6097–6112.
- Lapusta, N., J. Rice, Y. Ben-Zion, and G. Zheng (2000), Elastodynamic analysis for slow tectonic loading with spontaneous rupture episodes on faults with rate- and state-dependent friction, *J. Geophys. Res.*, **105**, 23,765–23,789.
- LeVeque, R. (2002), *Finite Volume Methods for Hyperbolic Problems*, Cambridge Univ. Press, Cambridge, U. K.
- Li, Y.-G., K. Aki, D. Adams, A. Hasemi, and W. H. K. Lee (1994), Seismic guided waves trapped in the fault zone of the Landers, California, earthquake of 1992, *J. Geophys. Res.*, **99**, 11,705–11,722, doi:10.1029/94JB00464.
- Madariaga, R., K. Olsen, and R. Archuleta (1998), Modeling dynamic rupture in a 3D earthquake fault model, *Bull. Seismol. Soc. Am.*, **88**, 1182–1197.
- Mase, C., and L. Smith (1985), Pore-fluid pressures and frictional heating on a fault surface, *Pure Appl. Geophys.*, **122**, 583–607.
- Mase, C., and L. Smith (1987), Effects of frictional heating on the thermal, hydrologic, and mechanical response of a fault, *J. Geophys. Res.*, **92**, 6249–6272.
- Moczo, P., J. Kristek, M. Galis, P. Pazak, and M. Balazovjeh (2007), The finite-difference and finite-element modeling of seismic wave propagation and earthquake motion, *Acta Phys. Slovaca*, **57**(2), 177–406.
- Oglesby, D., R. Archuleta, and S. Nielsen (1998), The three-dimensional dynamics of dipping faults, *Bull. Seismol. Soc. Am.*, **90**, 616–628.
- Oglesby, D., R. Archuleta, and S. Nielsen (2000), Earthquakes on dipping faults: The effects of broken symmetry, *Science*, **280**, 1055–1059.
- Olsen, K., R. Madariaga, and R. J. Archuleta (1997), Three-dimensional dynamic simulation of the 1992 Landers earthquake, *Science*, **278**(5339), 834–838.
- Pelties, C., M. Käser, V. Hermann, and C. E. Castro (2010), Regular versus irregular meshing for complicated models and their effect on synthetic seismograms, *Geophys. J. Int.*, **183**(2), 1031–1051, doi:10.1111/j.1365-246X.2010.04777.x.
- Poliakov, A. N. B., R. Dmowska, and J. R. Rice (2002), Dynamic shear rupture interactions with fault bends and off-axis secondary faulting, *J. Geophys. Res.*, **107**(B11), 2295, doi:10.1029/2001JB000572.
- Rice, J. R. (1999), Flash heating at asperity contacts and rate-dependent friction, *Eos Trans. AGU*, **80**(46), Fall Meet. Suppl., F681.
- Rojas, O., E. M. Dunham, S. Day, L. Dalguer, and J. Castillo (2009), Finite difference modelling of rupture propagation with strong velocity-weakening friction, *Geophys. J. Int.*, **179**, 1831–1858.
- Ruina, A. L. (1983), Slip instability and state variable friction laws, *J. Geophys. Res.*, **88**, 10,359–10,370.
- Sherwin, S. (2000), Dispersion analysis of the continuous and discontinuous Galerkin formulation, paper presented at International Symposium on Discontinuous Galerkin Methods, Salva Regina Coll., Newport, R. I.
- Tada, T., and R. Madariaga (2001), Dynamic modelling of the flat 2-D crack by a semi-analytic BIEM scheme, *Int. J. Numer. Methods Eng.*, **50**(1), 227–251, doi:10.1002/1097-0207(20010110)50:1<227::AID-NME166>3.0.CO;2-5.
- Titarev, V., and E. Toro (2002), ADER: Arbitrary high order Godunov approach, *J. Sci. Comput.*, **17**(1–4), 609–618.
- Toro, E. (1999), *Riemann Solvers and Numerical Methods for Fluid Dynamics*, Springer, Berlin.
- Vilotte, J.-P., G. Festa, and J.-P. Ampuero (2006), Dynamic fault rupture propagation using nonsmooth spectral element method, *Eos Trans. AGU*, **87**(52), Fall Meet. Suppl., Abstract S52B-05.
- Wald, D., and T. Heaton (1994), Spatial and temporal distribution of slip for the 1992 Landers, California, earthquake, *Bull. Seismol. Soc. Am.*, **84**, 668–691.

J.-P. Ampuero, Seismological Laboratory, California Institute of Technology, 1200 E. California Blvd., MC252-21, Pasadena, CA 91125, USA.

G. B. Brietzke, Department of Physics of the Earth, German Research Centre for Geosciences, Helmholtzstr. 7, D-14467 Potsdam, Germany.

J. de la Puente, Department of Computer Applications in Science and Engineering, Barcelona Supercomputing Center, Torre Girona, C/ Jordi Girona 31, E-08034 Barcelona, Spain.

M. Käser, Geo Risks Research, Münchener Rückversicherungs-Gesellschaft, Königinstr. 107, D-80802 München, Germany.

C. Pelties, Geophysics Section, Department of Earth and Environmental Sciences, Ludwig-Maximilians-Universität, Theresienstr. 41, D-80333 München, Germany. (pelties@geophysik.uni-muenchen.de)